Thermomechanical residual stress evaluation in multi-crystalline silicon solar cells of photovoltaic modules with different encapsulation polymers using synchrotron X-ray microdiffraction

Sasi Kumar Tippabhotla[1], Noel G. Diesta[2], Xingui Zhang[2], Shankar Sridhara[2], C. V. Stan[3], N. Tamura[3], Andrew A. O. Tay[1], A. S. Budiman[1,*]

[1]Xtreme Photovoltaics Laboratory (XPV Lab),
Singapore University of Technology and Design, Singapore 487372

[2]Cells and Module Technology Division
REC Solar Pte. Ltd., Singapore 637312

[3]Advanced Light Source (ALS)
Lawrence Berkeley National Laboratory (LBNL), Berkeley, CA 94720.

*suriadi@alumni.stanford.edu

Abstract

Photovoltaic (PV) module reliability issues due to silicon cell cracking is gaining more and more attention due to increasing demand for solar power and reduction of cell thickness to reduce cost. Recent reports show significant effect of encapsulation polymer material on cell cracks leading to the idea of tailoring encapsulation materials for more reliable PV modules. This paper investigates the effect of encapsulation modulus on the cell residual stress using Synchrotron scanning X-ray microdiffraction (μSXRD), which has been proven to be an effective technique to probe the stress in silicon solar cells, especially once they are encapsulated. The post lamination residual stress in the encapsulated multi-crystalline silicon (mc-Si) solar cells was reported for the first time using μSXRD in this manuscript and provide quantitative evaluation of the effect of encapsulation modulus on the cell residual stress. Further simple approximate finite element (FE) model was also developed to evaluate the effect of the encapsulation polymer on the cell stress. The FE simulations predict the trend of the stress variation with encapsulation polymer modulus very well. Dynamic mechanical analysis and rheological testing of the encapsulation polymers was also performed to correlate the polymer behaviour with the experimental and simulated stresses. Both experimental and simulation results show a similar trend of significant cell stress variation with encapsulation polymer modulus. In the case of external loading, the temperature of load application is observed to be very significant as it dictates the elastic state of the encapsulant, leading to critical conclusion that the encapsulant needs to be selected based elastic behaviour over the temperature history of the encapsulant during module fabrication and operation. The results and discussion presented are expected to be very useful for development of more reliable PV modules.

1. Introduction

Fracture of crystalline silicon solar cells in photovoltaic (PV) modules is widely reported and a well-known issue in the PV industry [1-2]. The PV module is a multilayer laminate of dissimilar materials bonded thermally. In such laminates, there will be built-in stresses (residual stresses) in the individual layers which may increase upon external loading and cause fracture and failure. In the case of solar

PV modules, the effect of soldering induced stresses was widely studied [3-4]. The effect of lamination (encapsulation) and encapsulation polymers on cell cracks was not given enough importance as the encapsulation polymers are very soft and flexible materials compared to the other constituent materials such as silicon, copper and glass. However recent reports have shown that the material properties and thickness of the encapsulation polymers strongly influence the stress and cracking of silicon cells in the modules [5-10]. Mickiewicz *et al*. [5] demonstrated strong dependence of cell cracks on the encapsulation polymer modulus at the loading temperature through static and dynamic load tests on modules made of ethylene vinyl acetate co polymer (EVA) and Silicone encapsulants. EVA is the most common commercial encapsulant but stiffer than Silicone, which is a less common but soft and costly material. Finite element analysis (FEA) simulations by Dietrich *et al*. [6] indicated that the elastic modulus variation during post lamination cooling of the PV module affected the module warpage and embedded cell gap, which they used as a metric for built-in stress in the module. Dietrich *et al*. [7] also demonstrated that a soft EVA encapsulant would lead to lower failure probability of the module compared to a stiffer EVA. It should be noted that the properties of EVA can differ based on its manufacturer. Paggi *et al*. [8] reported that the cracked cells upon loading will recover after unloading due to the binding effect of the encapsulation polymer. Li *et al*. [9] used FEA to show that the stress in a Germanium solar cell PV module increased linearly with the modulus, thickness and curing temperature of the encapsulation polymer. Handara *et al*. [10] compared mini PV modules made of monocrystalline silicon interdigitated back contact (IBC) solar cells using Synchrotron scanning X-ray microdiffraction (μSXRD) measurements of stress to show that a stiffer encapsulant caused more stress in the cell than a softer encapsulant. They also used fracture testing to prove the point further. Our recent work, Tippabhotla *et al*. [11] on residual stress evolution in IBC silicon solar cells using both μSXRD experiments and FEA showed that the stress concentrates near the solder joint with the copper ribbon due to local deformation of the cell. This local deformation of the cell is a result of the vacuum pressure applied on the cell during lamination process. Due to the adhesive nature of the encapsulant, this local deformation of the cell is retained even after lamination process, which binds the cell to the stiffer front glass. Hence, the properties of the encapsulant effects the stress in the cell.

With the above review of literature, it is very clear that the encapsulant plays a vital role in the cracking of silicon cells, which means, a properly selected or tailored encapsulant can make the PV modules more resistant to cell cracking and associated degradation. However, the reported research is either based on probability of fracture or crack statistic upon external loading considering only a few encapsulants or simulations. Other reports [10, 11] have used the μSXRD technique to investigate stress in encapsulated single crystalline silicon solar cells and demonstrated its effectiveness in probing mechanical stress in encapsulated silicon solar cells. In the current work, for the first time, an attempt was made to evaluate the effect of encapsulant modulus and thickness on the post lamination residual stress in a polycrystalline silicon (mc-Si) solar cells with REC Solar, using μSXRD. The unique capability of this approach is the quantitative evaluation of highly localized stress in the cell near the solder joint (cell to copper ribbon joint, Figure 1c). This is where the stress is concentrated and cracks originate (or existing micro cracks propagate) in the solar cells [3-4]. Five different commercially available encapsulation polymers were used in this study to get a systematic understanding of the effects. Further the effect of thickness of the encapsulant, EVA was also studied. A simple representative 2D FEA simulation was also performed to elucidate the mechanics of the residual stress evolution during the module integration process from soldering to lamination.

2. Experimental

2.1 Experimental Samples

Mini PV module samples with single mc-Si solar cell, as shown in Figure-1 were fabricated at REC Module Technology Laboratory for this experimental study.

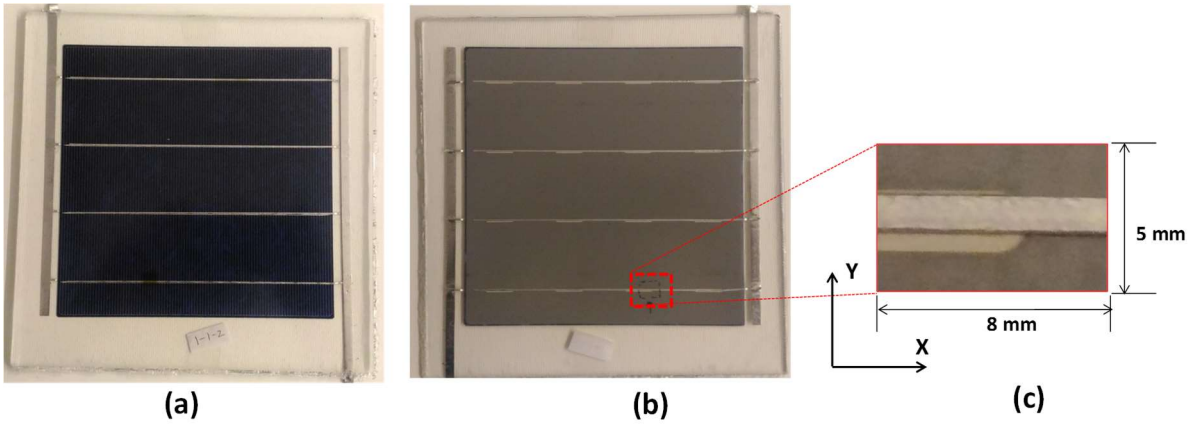

Figure 1: Mini PV module sample – (a) Front side, (b) Back side, (c) µSXRD scan region

This experiment was divided into two different case studies based on the literature reviewed.

1. Case Study 1: Effect of encapsulation polymer modulus on cell residual stress
2. Case Study 2: Effect of encapsulation polymer (EVA) thickness on cell residual stress

Hence two sets of single cell mini module samples were prepared as shown in the Table-1 below to cater the case studies 1 and 2. The cells used in this study were mc-Si cells of 156 X 156 mm^2 area and thickness 0.18 mm, with 4 busbars, soldered in the REC module fabrication line, which is fully automated. The front glass used in the mini modules was a typical mini-module glass plate of area 200 X 200 mm^2 with 3.2 mm thickness. A back sheet was not used in the mini modules as the cell needed to be visible from back side for the µSXRD experiments. The lamination process was carried out at a temperature of 160 ^oC, under 0.1 MPa vacuum pressure for 13 min, which is typical for REC PV modules. The details of the encapsulants such as name, chemical formula etc. are proprietary information and cannot be disclosed, hence they are arbitrarily named as Encap1 to Encap5 as shown in Table-1.

Table 1: Encapsulant details of experimental mini PV modules

Sample Set No.	Sample No.	Encapsulation Polymer		Encapsulation Polymer Thickness (mm)	
		Front	Back	Front (t_{fe})	Back (t_{be})
1	1-1	Encap-1	Encap-2	0.45	0.45
	1-2	Encap-3	Encap-3	0.45	0.45
	1-3	Encap-4	Encap-2	0.45	0.45
	1-4	Encap-5	Encap-5	0.45	0.45
2	2-1	EVA	EVA	0.6	0.45
	2-2	EVA	EVA	0.45	0.45

2.2 Synchrotron X-ray Microdiffraction (µSXRD) Experiments

According to Bragg's law [12-13], a crystalline material sample subjected to X-rays, produce diffraction patterns, which can be analysed to evaluate crystal structure, orientation and deformation (strain). At the Advanced Light Source (ALS), a synchrotron facility at Lawrence Berkeley National Laboratory (Berkeley Lab, CA., USA), a microdiffraction beamline end station (BL 12.3.2) capable of producing a high energy (5-26 keV) polychromatic X-ray beam of 1 µm diameter is available [13-15]. The beamline produces highly focused, high flux X-rays generated by a superbend magnet source and specialized focusing optics [14-16]. Very high spatial resolution stress measurements are possible with this microdiffraction BL 12.3.2 [17] and such capability is essential for very local residual stress evaluation near soldered copper interconnects in encapsulated mc-Si cells. A detailed description of the microdiffraction beamline is given elsewhere [14-17]. The efficacy of synchrotron X-ray diffraction in enabling technologically important innovations, including in microelectronics and nanotechnology industries, in additions to next generation silicon solar PV technologies, have recently been reported and described elsewhere [18-22]

Figure 2a shows the schematic of the microdiffraction experiment setup and an actual picture of the setup is shown in Figure 2b. The sample was mounted on the stage with its back (Figure 1b) facing the X-ray beam, as X-rays cannot penetrate the front glass due to absorption. To focus the X-ray beam on the cell, the back sheet was omitted in the mini PV module samples. In this setup, the sample was mounted at 45° to the X-ray beam, which is horizontal and a hybrid pixel area detector (DECTRIS Pilatus 1M) which is mounted above the sample records the 2D diffraction patterns from it. Hence this setup can record multiple diffraction peaks satisfying Bragg's condition in a single exposure to polychromatic X-ray beam (white beam), also called Laue diffraction [17] and the resulting diffraction pattern is called Laue Pattern or Laue-gram. Further the sample stage could move in X, Y and Z directions, enabling raster scanning. The sample was placed in the XY plane and the Z direction was normal to the sample plane [23] and the stage was adjusted to focus the X-ray beam on the sample per the experimental requirement by moving in Z-direction, so that movement in the XY plane did not alter the focus of the X-ray beam. Then, the sample was scanned using a 100µm displacement step along the X and Y directions. The actual scanned region is shown in Figure 1c, which is an envelope of ~4000 scan points with 1.5 sec exposure at each point, requiring around 2.5 to 3 hours for each scan.

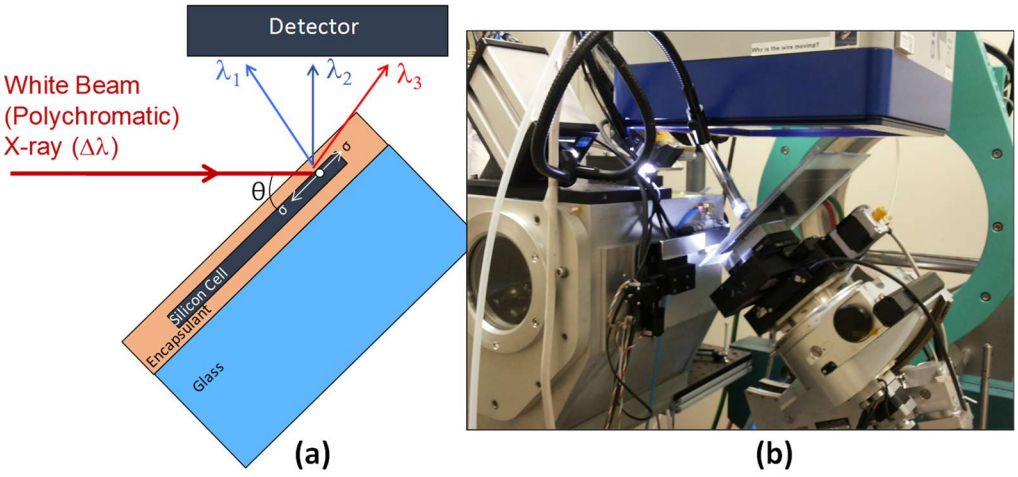

Figure 2: µSXRD setup of mini PV module (a) Schematic, (b) Actual picture

The resulting Laue patterns can be analysed by the specialized XMAS software [23], which uses a peak fitting routine to identify each diffraction peak, and attribute the *h k l*, Miller indices in a process called indexing. The indexing provides the orientation of the crystal. The accuracy of the crystal orientation depends on the number of peaks indexed, which in turn depends on the position, area and sensitivity of the area detector. In the present experiment, a threshold of 20 indexed peaks was considered i.e., if the number of indexed peaks at any scan point is less than 20, that point was considered to have no signal. This is because, the white X-ray beam penetrates though the silicon cell (thickness 180 µm) [10, 24] but it cannot pass through thick copper and solder near the solder joints, ref. Appendix A of Ref. [10]. Further our previous work on residual stress evaluation of encapsulated single crystal silicon IBC cells using µSXRD [10, 11, 25, 26] can be referred for more detailed description of the experimental procedure, Laue pattern analysis and stress evaluation. However, these previous works adopt a curvature based stress evaluation which is more accurate but possible due to single crystal cells. Since the entire scanned region of the cell is one crystal, the change in the orientation of the crystal within the scanned region can be used to estimate the local curvature. The curvature can then be used to calculate the bending strain and stress later. In the case of the current multi crystalline cell, there can be several grains of different orientations within the scanned region hence, local grain mis-orientation will lead to erroneous results at grain boundaries. Hence a slightly different method was adopted to evaluate the stress, as explained below [23].

A minimum of 5 peaks need to be indexed in the Laue pattern to identify the crystal structure of the grain, but more peaks will improve the orientation and strain accuracy. Once the crystal has been indexed, the deformed and un-deformed crystal structures can be related by the homogeneity property [23] i.e., the coordinates of an arbitrary point in an un-deformed unit cell remain unaffected in the deformed unit cell. Based on this condition, the deviatoric stress can be calculated as explained in [23, 10, 26].

The deviatoric stress is given by the Equation (1) and the same in matrix form is given by Equation (2) below.

$$\sigma'_{ij} = \sigma_{ij} - \sigma_H \delta_{ij} \tag{1}$$

or

$$\begin{bmatrix} \sigma'_{11} & \sigma_{12} & \sigma_{13} \\ \sigma_{21} & \sigma'_{22} & \sigma_{23} \\ \sigma_{13} & \sigma_{32} & \sigma'_{33} \end{bmatrix} = \begin{bmatrix} \sigma_{11} & \sigma_{12} & \sigma_{13} \\ \sigma_{21} & \sigma_{22} & \sigma_{23} \\ \sigma_{31} & \sigma_{32} & \sigma_{33} \end{bmatrix} - \sigma_H \begin{bmatrix} 1 & 0 & 0 \\ 0 & 1 & 0 \\ 0 & 0 & 1 \end{bmatrix} \tag{2}$$

where σ_H is, the hydrostatic stress given by the Equation (3) below.

$$\sigma_H = \frac{\sigma_{ii}}{3} = \frac{\sigma_{11}+\sigma_{22}+\sigma_{33}}{3} \tag{3}$$

Only deviatoric stress can be calculated by Laue diffraction and to calculate the total stress, we need hydrostatic stress as shown by Equation (1) or (2). Calculation of hydrostatic stress require to evaluate the energy of one of the diffraction peaks by performing an energy scan using a monochromator [23]. The energy scan requires a few minutes at each scan point, which means the time of total scan increases to days. Owing to the limited beamtime allocation to each user group in a cycle, this is rather impossible. However, the thin plate structure of the mc-Si cell let us conveniently assume plane stress condition, leading to stress along the thickness of the cell (along direction 3) to be zero, i.e.,

$$\sigma_{33} = 0 \tag{4}$$

Substituting Equation 4 in Equation 1, the hydrostatic stress can be calculated as shown in Equation 5 below and substituting it in Equation 1 will give the full stress tensor at each scan point [23]

$$\sigma'_{33} = \sigma_{33} - \sigma_H = -\sigma_H \quad (5)$$

The indexing and stress calculation process of each Laue pattern of the scan can be automated using XMAS [23] and finally a map of output quantity such as grain orientation, strain, stress etc. over the scanned region can be generated. The stress maps thus generated are presented in the Section 4.

2.3 Encapsulation Polymer Characterization

The encapsulation polymers used in this work are characterized by DMA and before and after curing. Cured polymers were obtained by laminating a few layers of polymers with the lamination recipe used for making the mini PV modules (ref. Section 2.1). TA800 DMA tester was used in film tension mode for the testing. The load was applied at 1 Hz frequency and the temperature was ramped from -60 ^{o}C to 150 ^{o}C with a ramp rate of 5 ^{o}C/min. The mechanical properties such as storage modulus, loss modulus and tan δ were evaluated as a function of temperature. Additionally, the viscosity of the raw polymers was also measured using TA DHA-2 rheometer from meting point (~80 ^{o}C) to the max lamination temperature (160 ^{o}C) to evaluate the tendency of low (relaxation) of the polymers during melting (or softening) and cross linking, which is difficult to measure with film tension mode in DMA. The results of the DMA and rheology testing were discussed in Section 4.

3. Finite Element (FE) Model and Simulations

A simple 2D FE model with plane-strain approximation was developed to represent a local portion of the mini PV module cross section as shown in the schematic in Figure 3 below. Since the geometry and loading around the cell with soldered copper ribbon during the module integration is symmetric, this simple model is expected to simulate the localized residual stress evolution in the cell near the soldered copper (Cu) ribbon. Actual FE model and mesh details are shown in Figure 4. The FE model was meshed with 8-node quadrilateral elements with quadratic shape functions using commercial FE code, ABAQUS V.6.14 [27]. The interfaces between cell and Cu ribbon, encapsulant and glass were simulated by tie constraints and the interfaces between cell / Cu ribbon and encapsulant are simulated by standard surface to surface contacts which don't separate once in contact. Solder between interconnect and the cell was not modelled in this simulation. All the materials used in the model were assumed to be isotropic and linearly elastic as shown in the Table 2 [11] except the copper ribbon. It was observed that the copper ribbon undergoes considerable yielding during soldering and hence elastic plastic properties were considered as shown in Table 3 [11]. The encapsulant is also assumed to be elastic and the measured storage modulus (Figure 5) was used as the elastic modulus. Though this model doesn't consider the melting of the encapsulant, the temperature varying storage modulus reduces to a negligible value (~ 0.6 MPa), which was shown to approximate the behaviour well [11].

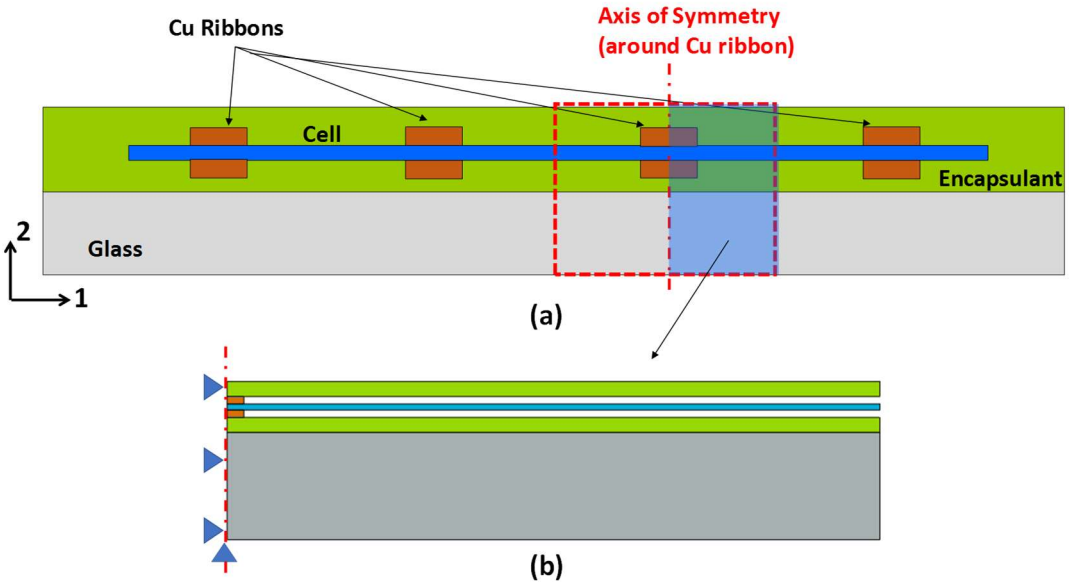

Figure 3: Schematic of (a) mini PV module cross section, across Cu ribbons (not to scale), (b) 2D FE Model (to scale)

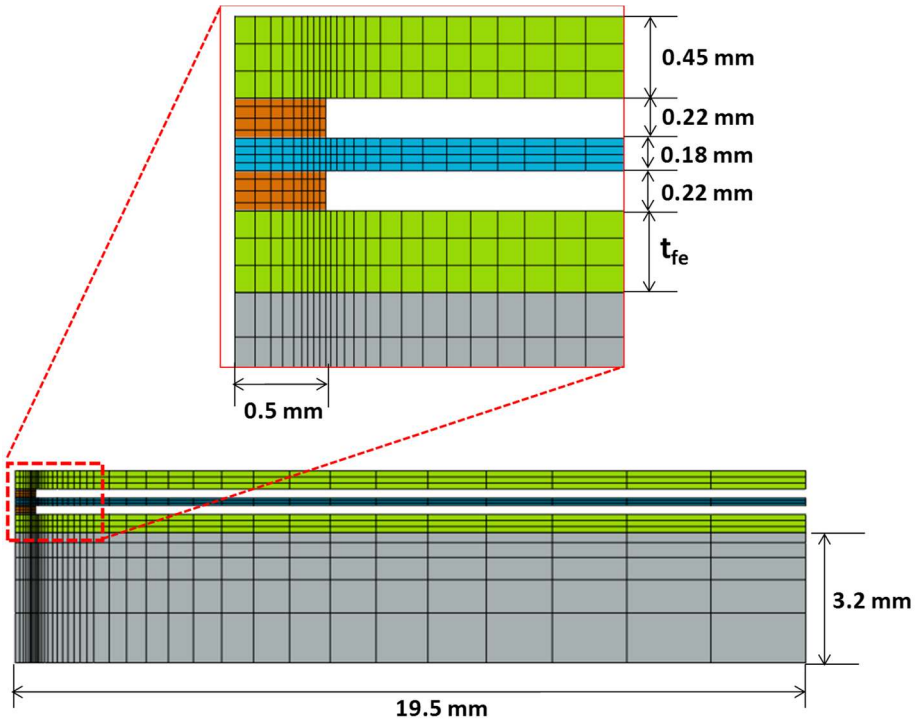

Figure 4: 2D FE model and mesh details, check Table 1 for 't_{fe}'

Table 2: Elastic material properties used in FE simulations

Material	Young's Modulus, E (GPa)		Poisson's Ratio	CTE (mm/mm/°C)	
	Value	Temperature (°C)		Value	Temperature (°C)
Silicon	130	---	0.28	1.72E-06	-53
				2.23E-06	-13
				2.61E-06	27
				2.92E-06	67
				3.34E-06	147
Copper (Interconnect)	91.5	-40	0.3	1.70E-05	---
	85.7	25			
	82	125			
	79.2	225			
Glass	73	---	0.235	8.00E-06	---
Encapsulant	Storage modulus from DMA was used (refer Section 4)		0.4	2.70E-04	---

Table 3: Elastic-plastic material properties of copper used in FE simulations

Yield Stress (MPa)	Tangent Modulus (MPa)	Temperature (°C)
116.2	1000	-40
95.1	1000	25
82	1000	125
79.2	1000	225

The PV module fabrication process was simulated in 2 steps as explained below [11].

1. Soldering with Cu ribbons: CTE mismatch from soldering temperature, 210 °C to room temperature, 25 °C. Only the cell and the copper ribbons on the top and bottom of the cell were present in this step of the simulation. It should be noted that the actual soldering temperature is above 220 °C, where the solder is in molten state and it attains reasonable stiffness at 210 °C.
2. Lamination of PV Module: The lamination process was simulated in the following 5 sub-steps as shown below
    a. Preheating to 50 °C
    b. Hot Press - vacuum pressure (0.1 MPa) application to remove air bubbles
    c. Heating to lamination temperature, 160 °C.
    d. Removal of vacuum pressure
    e. Cooling to room temperature, 25 °C.

Subsequently, an external load of 2.4 MPa was applied on the module at different temperatures to evaluate the effect of encapsulants on external load transfer.

All the simulation steps were carried out assuming steady state conditions. The soldering step is important in the simulation as it captures the initial residual stress in the silicon cell before lamination and the Cu ribbon undergoes considerable yielding during lamination [28] and its stiffness decreases in subsequent simulation steps. During the lamination process, the silicon cell undergoes bending under the vacuum pressure due to the front Cu ribbon height, leading to higher bending stresses in the cell near the ribbon. This stress relaxes to a lower value upon heating to lamination temperature

due to softening and expansion of the encapsulant but increases to a higher value as the laminate cools down to room temperature.

4. Results & Discussion

4.1 Characterization of Encapsulants

Figure 5 shows the variation of the storage modulus of the cured encapsulation polymers considered in this study with temperature. All the polymers appear to have a similar storage modulus value at high temperature above 100 °C but as the temperature decreases, the modulus values tend to increase differently for different polymers. Encapsulant 5 is stiffer in the temperature range from 20 °C to 100 °C and Encapsulant 3 is softer in the same range. However, it can be noticed that the Encapsulants 2, 3 and 4 have very small differences in their storage modulus from 20 °C to 100 °C. But below 20 °C, the storage modulus of all the encapsulants tend to increase steeply due to glass transition except Encapsulant 4, which has very distinctly low storage modulus throughout the range of temperatures considered.

Storage modulus gives insight into how the polymer behaves during post lamination cooling and thereafter. However, it is also essential to understand the behaviour of the polymer during the lamination heating process as the polymer melts (or softens) under heat and start to cross-link (in case of thermosetting polymers such as EVA). Due to these changes in the polymer, the vacuum pressure load transfer to the cell will be affected. Figure 6 shows the viscosity of the uncured encapsulants during curing from 80 °C to 160 °C. The viscosity of the Encapsulant 5 was not shown as it did not melt even at 160 °C. It only softened above 130 °C, enabling adhesive bonding under pressure, so it appears to exhibit a stiff thermoplastic behaviour below 160 °C. Encapsulant 4 also appears to exhibit thermoplastic behaviour as its viscosity decreases till 150 °C and only a marginal increase is noticed beyond that and it has the lowest viscosity among the 5 polymers considered. The viscosity of Encapsulants 1 and 2 drop from 80 °C to 130 °C and at 140 °C, it tends to increase steeply, which is characteristic of thermosetting (crosslinking) polymers. They appear to solidify around 150 °C and beyond that the viscosity drop abruptly due to shearing of the solidified encapsulant layer between the rheometer plates. Encapsulant 3 also seems to exhibit thermosetting behaviour but it melts around 100 °C and show much higher viscosity compared to Encapsulants 1 and 2.

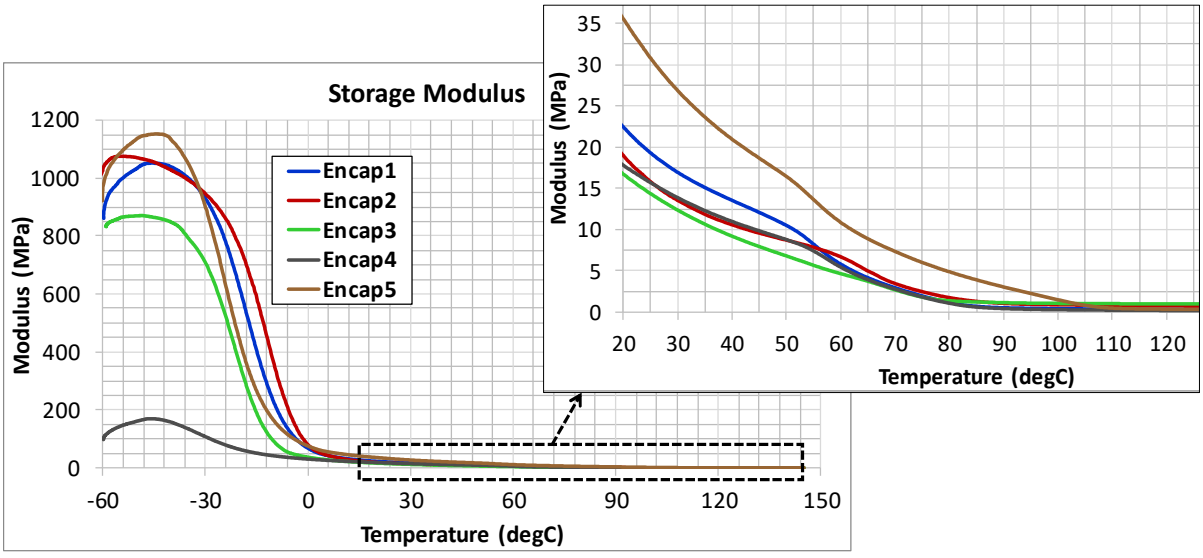

Figure 5: Storage modulus variation of the cured encapsulation polymers with temperature

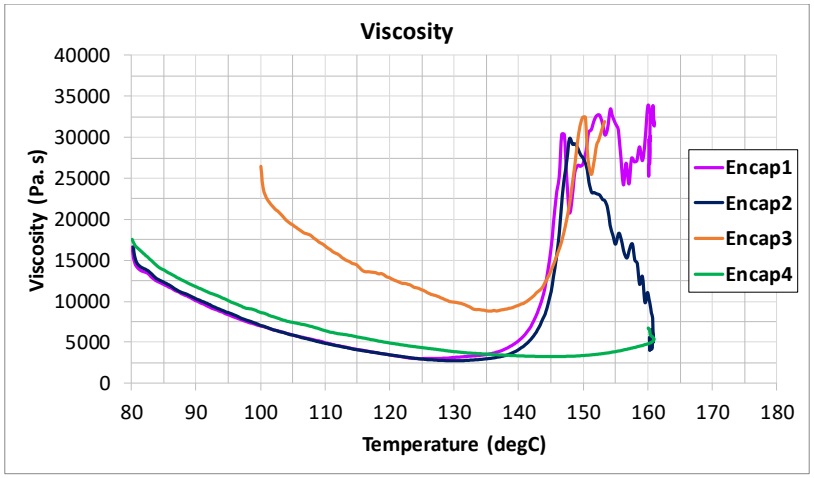

Figure 6: Viscosity of the uncured encapsulation polymers with temperature (Encapsulation polymer 5 did not melt at 160 °C)

4.2 Stress distribution measured using µSXRD

The stress maps (pertaining to the scan region in Figure 1c), obtained from µSXRD experiments on case study 1 (effect of encapsulant modulus) are shown in Figure 7. The magnitude of the cell residual stress in the Y-direction (across the copper ribbon) is different for different encapsulation polymers.

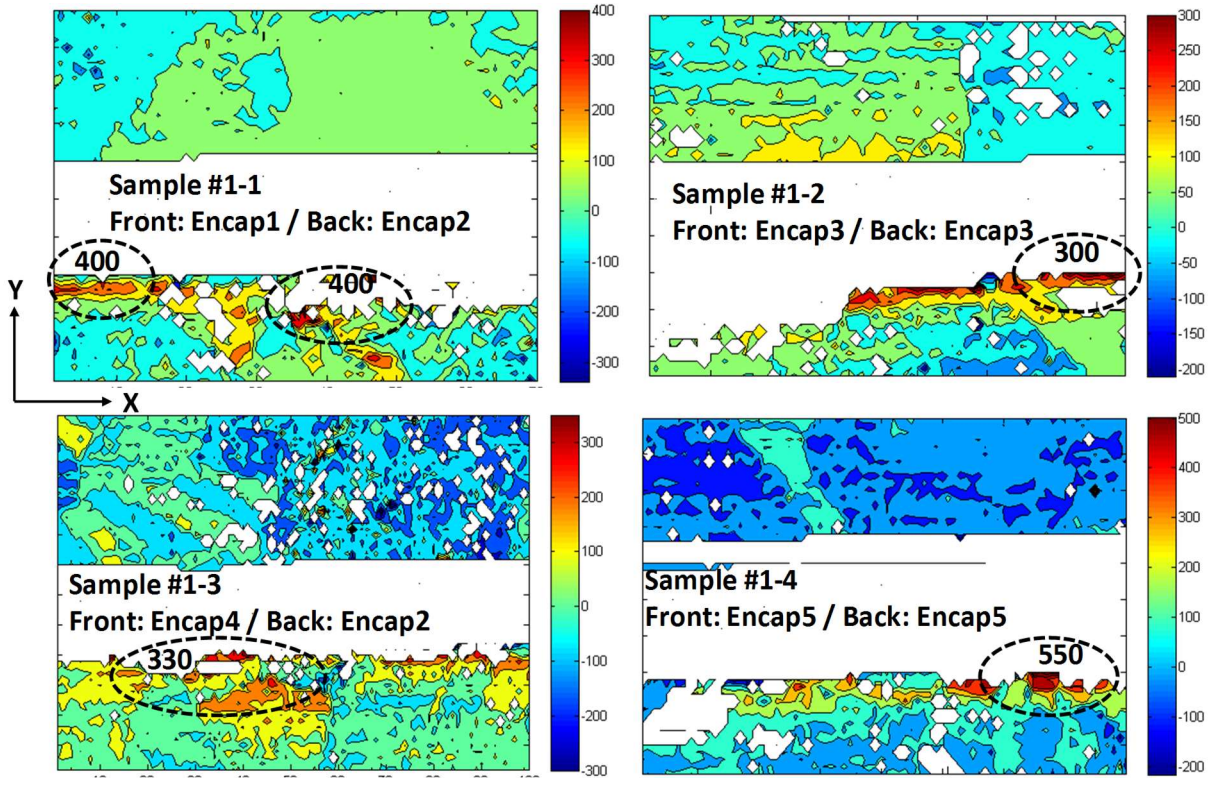

Figure 7: Cell residual stress (Y-direction) in different mini PV module samples from µSXRD experiments on case study 1 (Note: the white region in the middle of the stress maps indicate no signal from diffraction due to Cu ribbon/ solder), stress values are in MPa

Further, it can also be seen that the sample # 1-4, with Encapsulant 5 shows the highest cell residual stress, while the sample # 1-2, with Encapsulant 3 shows the lowest stress. Cell residual stress in the

sample # 1-3, with front Encapsulant 4 and back Encapsulant 2 also shows low stress. The residual stress in sample # 1-1, with front Encapsulant 1 and back Encapsulant 2 falls in between. The residual stress in the cells correlates well with the storage modulus of the encapsulants at room temperature, i.e., the sample with stiffer polymer (high storage modulus) has high residual stress in the cell and vice versa. The effect of encapsulant modulus on the cell residual stress is evident from this result and proves that the effect is significant.

Figure 8 shows stress maps obtained from the µSXRD experiments on case study 2 (effect of encapsulant, EVA thickness). The sample # 2-1 with thicker front encapsulant has lower cell residual stress compared to sample # 2-2 with thinner encapsulant. This result agrees with the electroluminescence (EL) images of full size modules with different EVA thicknesses after mechanical load testing (MLT) as shown in Figure 9.

Further the stress maps in Figures 7 and 8 show that the high stress in the cell is concentrated along the lower edge of the interconnect ribbon and no high stress along the upper edge is shown. This is due to the µSXRD experimental setup used. In reality, there will be high cell stress along both the edges of the interconnect ribbon. In our µSXRD experiments the cell region near the upper edge of the interconnect ribbon was shadowed by the thickness of the interconnect. Hence the X-ray beam was unable to reach there. Therefore, no diffraction signal from the cell region near the upper edge of the interconnect ribbon was recorded and hence the stress maps show high stress, only at the lower edge of the interconnect ribbon.

Since the solar cells used in this study were made of mc-Si, the stress maps were influenced by the orientation of the individual grains in the µSXRD scan region. The grain orientation maps are shown in Appendix-A, where the effect of the grain orientation on the stress is also discussed.

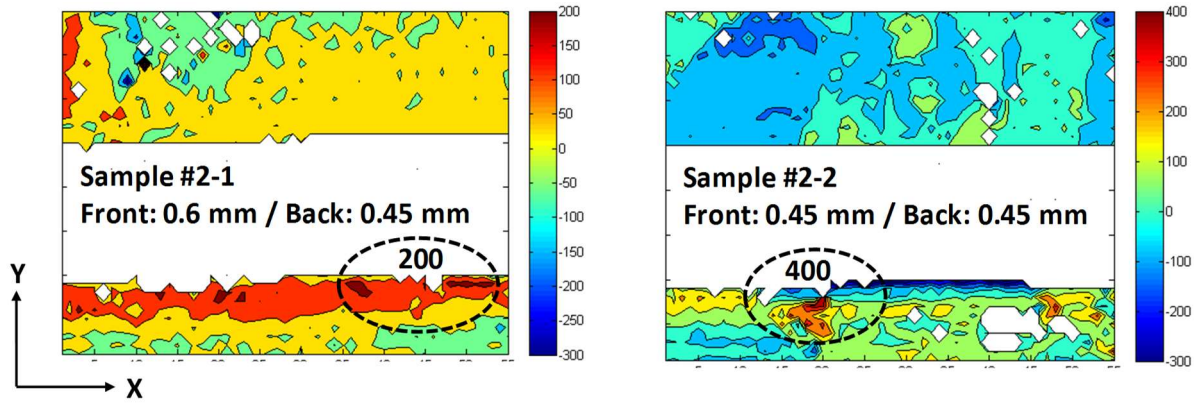

Figure 8: Cell residual stress (Y-direction) in different mini PV module samples from µSXRD experiments on case study 2 (Note: the white region in the middle of the stress maps indicate no signal from diffraction due to Cu ribbon/ solder), stress values are in MPa

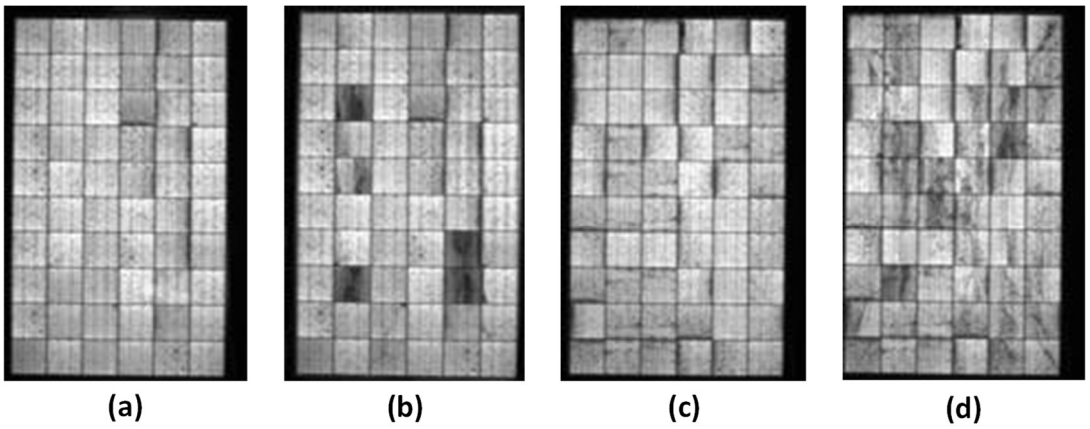

Figure 9: EL images of full size modules, (a) with thick EVA – before MLT, (b) with thick EVA – after MLT, (c) with thin EVA – before MLT, (d) with thin EVA – after MLT

4.3 Finite element simulations

The experimental results clearly establish the significant effect of encapsulant material on the post-lamination residual stress in the mc-Si cell, however, it cannot give information about the origin of the stress or the reason for such a high stress and how it gets affected by the encapsulant material. The FE simulations help to clarify this. Figure 10 below shows simulated residual stresses in the silicon cell at different stages of the module-making process for the model with Encapsulant 1. The stress plots in Figure 10 indicate that the maximum stress in the cell varies with each step of the lamination process. Due to mismatch of the coefficient of thermal expansion (CTE) of copper and silicon, residual stress develops in the cell upon cooling from soldering temperature to room temperature (RT), 25 ^{o}C, as shown in Figure 10a. Upon preheating to 50 ^{o}C during lamination, the maximum stress in the cell is slightly reduced (Figure 10b). Hot pressing (application of vacuum pressure, 0.1 MPa) leads to bending of the cell over the edge of the front ribbon (glass-side ribbon, bottom one in the stress plots) as shown in Figure 10c, which introduces high bending stress in the cell as shown. Upon further heating to lamination temperature, 160 ^{o}C, the encapsulant expands, softens (or melts and start to crosslink), relieving stress in the cell as shown in Figure 10d. At the end of the lamination process, the vacuum pressure is removed but, by then the encapsulant adhesively bonds with the interfaces and hence no difference in the cell stress is seen (Figure 10e). The final step in the process is cooling of the hot laminate to RT, during which the encapsulant stiffens, regaining its solid state and in the process, induces high bending stress in the cell as shown in Figure 10f. Upon external loading (uniform pressure of 2.4 MPa) at room temperature, the bending stress tend to further increase as shown in Figure 10g.

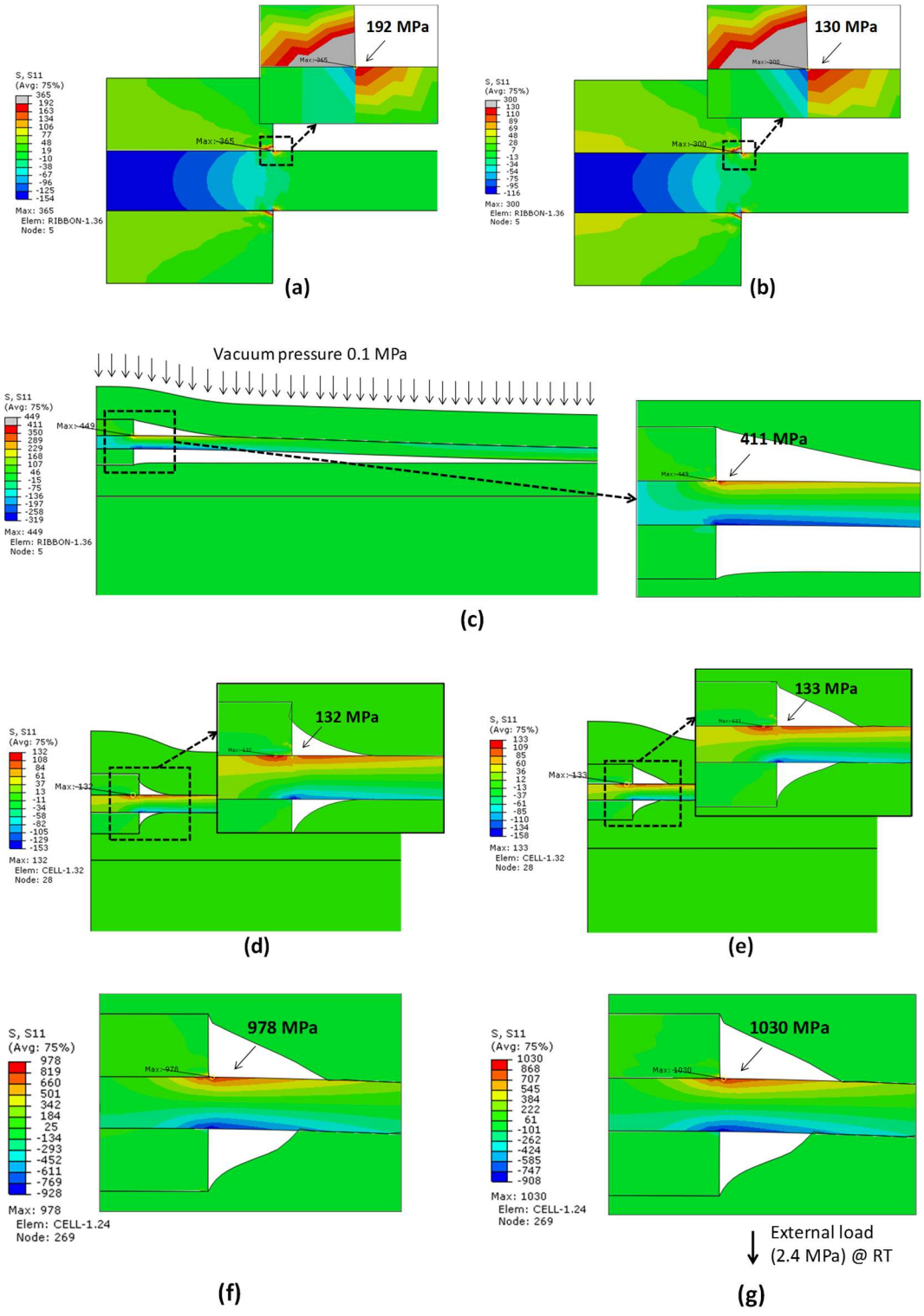

Figure 10: Silicon cell stresses (in the model with Encapsulant) 1 from FEA at, (a) Post soldering, (b) Lamination preheat to 50 °C, (c) Lamination Hot Press, (d) Lamination heating to 160 °C, (e) Vacuum pressure removal, (f) Post lamination, (g) External load 2.4 MPa @ room temperature (RT)

It should be noted that the absolute magnitude of the simulated stresses may not be very accurate due to the simplified 2D FE model used in the analysis, especially during lamination heating the encapsulant melts (or softens) filing the gaps at the corners of the Cu ribbon and silicon cell joints (ref.

Figures 10d – 10g) and this will relieve the stress in the cell partially. Hence the actual post-lamination stress values may be lower. If the encapsulant melts and flows like a liquid at lamination temperature, the bending stress induced in the cell due to hot pressing (Figure 10c) will be completely relieved. But the viscosity of the molten (or softened) encapsulant (ref. Figure 6) is very high (> 3000 Pa. s) even at max lamination temperature compared to that of liquids like oil (~ 0.1 Pa. s). Hence, the encapsulant acts as a viscous gel and allow only partial relaxation of the cell stress. In such a scenario, the simulated stress values from the present FE model are reasonably well expected to give the worst-case scenario, which can be used for comparative evaluation of different encapsulants and also help to look at the sensitivities of various design and lamination parameters in a systematic manner. Further, it will also help to look at the different stages of the manufacturing process to identify the critical step which requires optimization.

The behaviour of the simulated stresses in the silicon cell at different stages of lamination process as shown in Figure 10 was observed to be similar for all the encapsulants considered. The magnitude of the simulated cell stresses at different process stages for different encapsulants is shown in Figure 11. It is observed from the plot that the post lamination cell residual stress is significantly different for different encapsulants. The cell stresses at the remaining process stages are similar, showing no dependence on the encapsulant. This result clearly show that the cell residual stress upon cooling to RT is a function of encapsulant modulus. To further reinforce this point, a plot of the post-lamination cell residual stress as a function of the encapsulant storage modulus at RT is presented in Figure 12. A linear dependence of the cell residual stress on the encapsulant modulus is noticed from Figure 12. Hence Figure 12 gives a relative order of encapsulants in terms of the increasing cell residual stress, which matches very well with the experimental predictions shown in Figure 7.

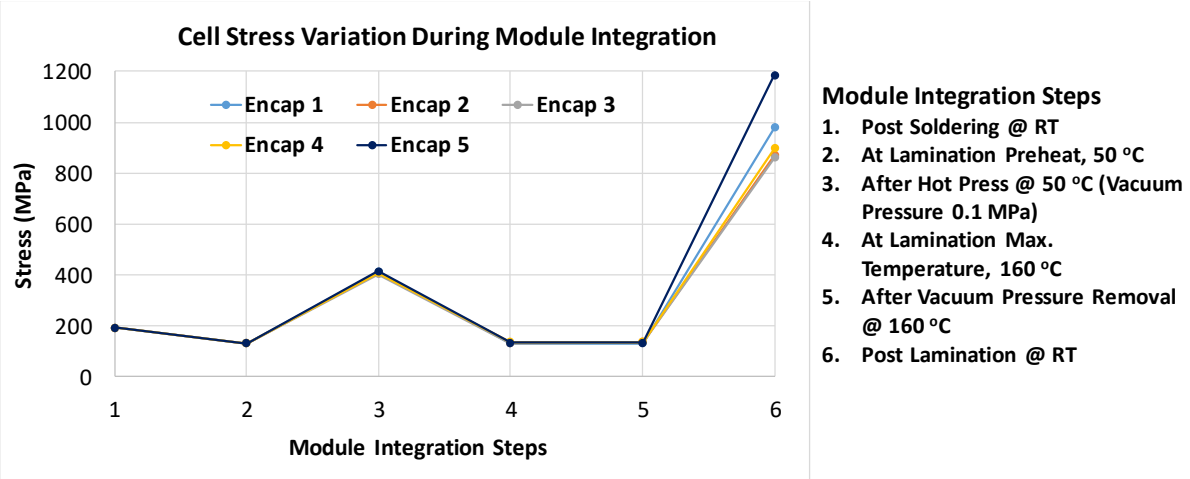

Figure 11: Variation of cell stress at different steps of module integration process for different encapsulants

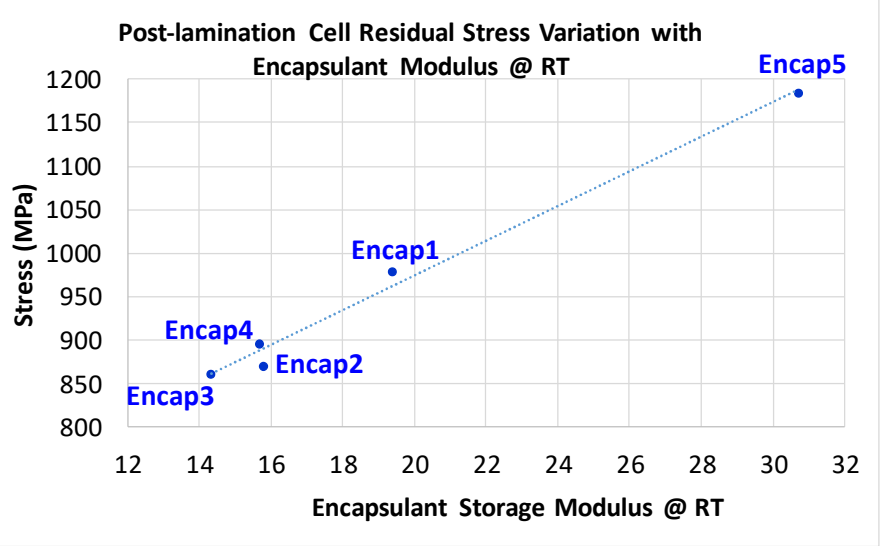

Figure 12: Post-lamination cell residual stress as a function of encapsulant storage modulus at RT

It would also be very important to evaluate the effect of the front and back encapsulants on the cell stress separately to address the optimization of module lamination more effectively. The post-lamination residual stress in the cell was simulated for different front encapsulants by keeping the back encapsulant to be Encapsulant 5. As shown in Figure 13, the post lamination cell residual stress is a function of front encapsulant storage modulus at RT. The stress variation is almost same as the case with same front and back encapsulants (Figure 12). Similarly, the post-lamination residual stress in the cell was simulated for different back encapsulants by keeping the front encapsulant to be Encapsulant 5. Figure 14 shows that the variation of cell residual stress with back encapsulant modulus at RT is almost negligible. Hence, the front encapsulant effect is more significant and it is reasonable as the front encapsulant transfer the constraints of CTE mismatch from the rigid glass to the cell during cooling to RT, whereas the back encapsulant doesn't in this case. However, in the case of a glass -glass module, both the encapsulants might affect the cell stress equally.

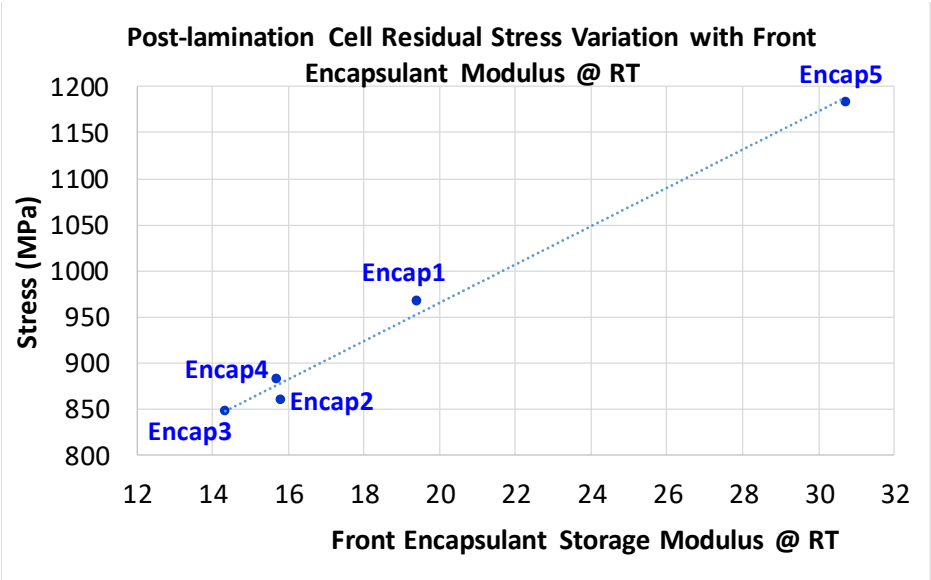

Figure 13: Post-lamination cell residual stress as a function of front encapsulant storage modulus at RT (back encapsulant is Encapsulant 5)

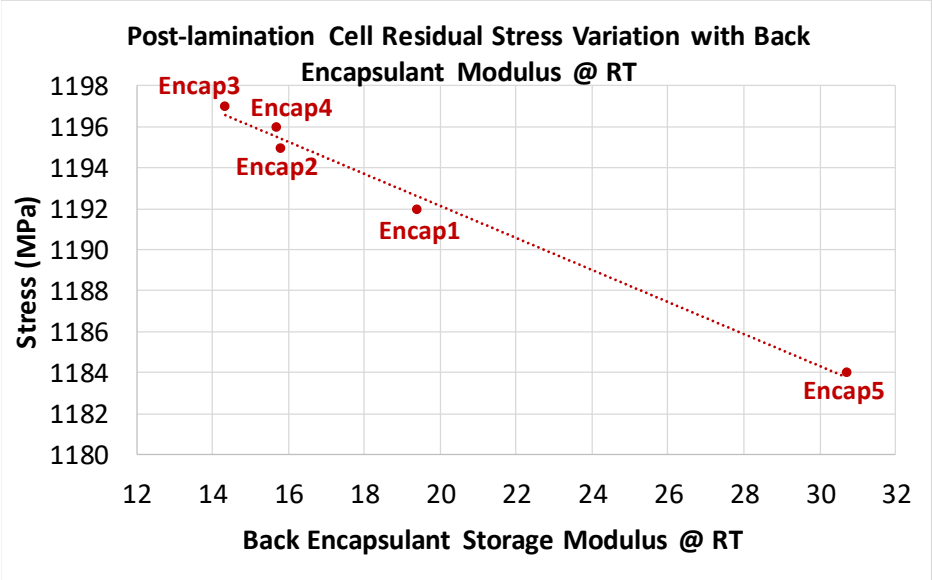

Figure 14: Post-lamination cell residual stress as a function of back encapsulant storage modulus at RT (front encapsulant is Encapsulant 5)

Further the cell stresses in the laminate subjected to an external uniform load of 2.4 MPa was simulated at two different temperatures, RT and -10 °C for different encapsulants. The plots of cell stress variation with the encapsulant modulus at the load application temperatures, RT and -10 °C are shown in Figures 15 and 16 respectively. Both the plots show that the cell stress is a strong function of the encapsulant modulus however, it can be noticed that the relative order of the encpsulants in terms of the increasing cell stress is different at different load application temperatures. This is due to the difference in the change of encapsulant modulus with decreasing temperature below RT. This indicates the complexity of encapsulant selection, as the encapsulant which is good at RT may not be good at lower temperatures. In the current scenario, Encapsulant 3 appears to be the better at RT however Encapsulant 4 actually gives lower cell stress, both at RT and below RT. Further from Figure 16 it can be noticed that the effect of the encapsulant modulus on the cell stress becomes less significant with the increasing encapsulant modulus. This is because, with the lowering temperature below RT, the modulus of the encapsulant increases to a higher value, losing its soft nature (glass transition). Hence, it tends to transfer all the load from the front glass to the cell like a rigid layer. With the onset of this rigid behaviour, the encapsulant loses its cushioning effect and its effect on the cell stress becomes less significant.

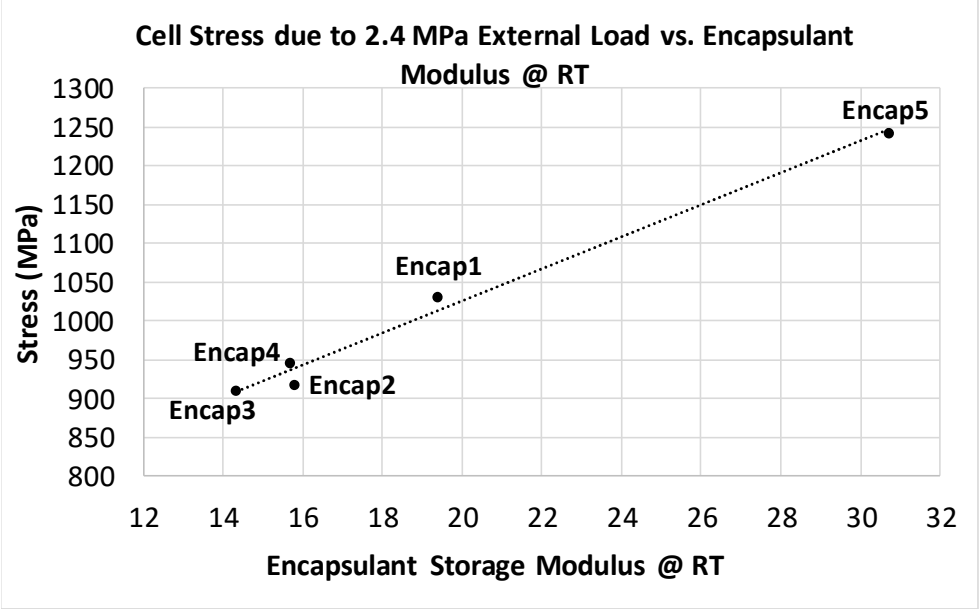

Figure 15: Cell stress due to 2.4 MPa external load (applied at RT) as a function of encapsulant storage modulus at RT

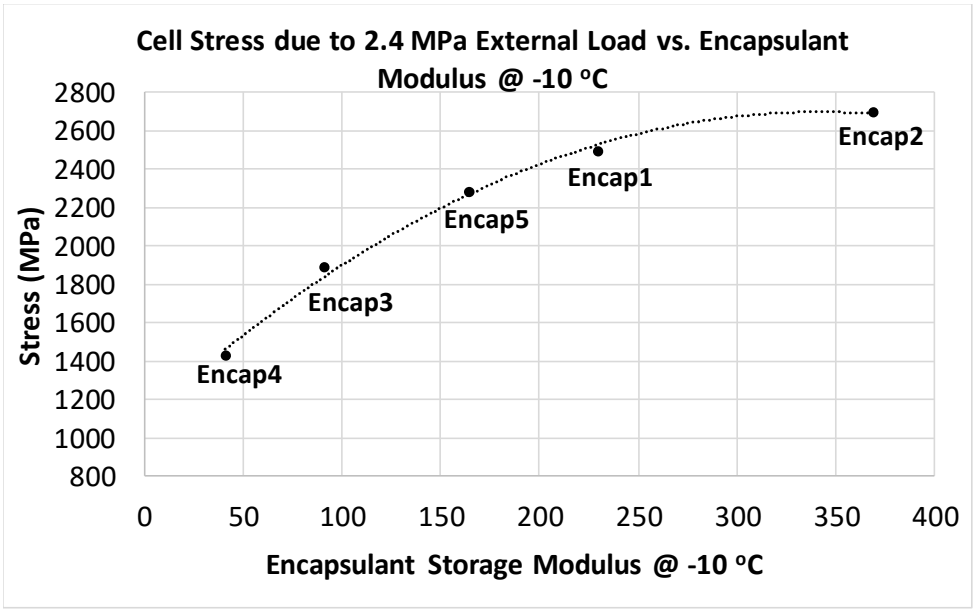

Figure 16: Cell stress due to 2.4 MPa external load (applied at -10 °C) as a function of encapsulant storage modulus at -10 °C

Conclusions

Residual stress in the encapsulated mc-Si cells measured using µSXRD was reported in this work for the first time. The effect of encapsulation polymers on the cell residual stress was evaluated using µSXRD experiments, polymer dynamic mechanical and rheological analyses and simplified approximate FE simulations. The experimental results show that the elastic modulus of different encapsulants vary significantly, especially between 80 °C and RT causing significant effects on the cell

residual stress after lamination as shown by the stress maps obtained from μSXRD. The stress maps obtained from μSXRD experiments also show that the thickness of EVA encapsulant has significant effect on the cell residual stress. Thicker the front encapsulant (EVA), smaller are the residual stresses. Further it was shown by FE simulations that the encapsulants that show rapid glass transition and steep raise of modulus below RT, causes the modules to experience significant cell stress under nominal external loading (Figure 16). Encapsulant 4 is soft with relatively moderate increase of modulus below RT, causing lower cell stress all throughout the temperature range considered. It was further shown with FE analysis that the front encapsulant has significant effect on cell stress whereas the back encapsulant effect is negligible. However, this may not be true for a glass-glass module. The FE model and simulation performed are in good agreement with the μSXRD experimental results in terms of the trend and can be used as a quick evaluation tool for new encapsulation materials. More accurate FE simulations with 3D FE model and advanced polymer properties are the subject of our continued investigations.

The results shown in this manuscript reinforce that the encapsulation polymer, though very compliant compared to the other constituent materials of the PV module (such as silicon, glass, etc.), can influence the cell stress significantly. Further a quantitative evaluation of the stress as a function of encapsulant modulus was presented in this manuscript through the unique μSXRD experiments and simplified FE simulations. This work is expected to enable selection of an appropriate encapsulation polymer to develop next generation highly reliable PV modules with lower cell residual stress.

Acknowledgements

S. K. Tippabhotla and A.S. Budiman would like to thank for collaboration, critical discussion and gratefully acknowledge the PV sample prototyping and laboratory facilities extended by REC Solar (Singapore).

S. K. Tippabhotla would also like to express sincere thanks to REC module technology laboratory personnel and leadership for help and support in sample, preparation and testing during internship.

S. K. Tippabhotla would also like to sincerely thank for discussion and support during rheological testing provided by Mr. Jeck Chuang Tan, PhD student, Singapore University of Technology and Design

The authors gratefully acknowledge the critical support and infrastructure provided by the Engineering Product Development Pillar, Singapore University of Technology and Design (SUTD).

S. K. Tippabhotla, and A.S. Budiman also gratefully acknowledge the funding and support from National Research Foundation (NRF)/Economic Development Board (EDB) of Singapore for the project under EIRP Grant **"(NRF2013EWT- EIRP002-017) - Enabling Thin Silicon Technologies for Next Generation, Lower Cost Solar PV Systems"**

The Advanced Light Source (ALS) (supported by the Director, Office of Science, Office of Basic Energy Sciences, and Materials Sciences Division, of the U.S. Department of Energy under **Contract No. DEAC02-05CH11231** at Lawrence Berkeley National Laboratory and University of California, Berkeley, California). The move of the micro- diffraction program from ALS beamline 7.3.3 onto to the ALS super-bend source 12.3.2 was enabled through the **NSF grant #0416243**.

References

1. Sander M, Dietrich S, Pander M, Schweizer S, Ebert, M, Bagdahn J. Investigations on crack development and crack growth in embedded solar cells, Proceedings SPIE 8112, Reliability of Photovoltaic Cells, Modules, Components, and Systems IV, 811209 2011. https://doi.org/10.1117/12.893662.
2. M. Köntges, S. Kajari-Schröder, I. Kunze, U. Jahn, Crack statistic of crystalline silicon photovoltaic modules, Proc. of 26th EUPVSEC, September 2011, Hamburg, Germany
3. Gabor M, et al. Soldering induced damage to thin Si solar cells and detection of cracked cells in modules. 21st European Photovoltaic Solar Energy Conference, 2006.
4. Wendt J, Träger M, Mette M, Pfennig A, Jaeckel B. The link between mechanical stress induced by soldering and micro damages in silicon solar cells, in: Proceedings of 24th EUPVSEC, 2009; 3420–3423.
5. R. Mickiewicz *et al.*, Effect of Encapsulation Modulus on the Response of PV Modules to Mechanical Stress, Proc. of 26th EUPVSEC, September 2011, Hamburg, Germany
6. Dietrich S, Pander M, Sander M, Schulze SH, Ebert M, Mechanical and thermomechanical assessment of encapsulated solar cells by finite-element-simulation, Proc. SPIE 7773, Reliability of Photovoltaic Cells, Modules, Components, and Systems III, 77730F, 18 August 2010. https://doi.org/10.1117/12.860661
7. Sascha Dietrich, Martin Sander, Matthias Pander, Matthias Ebert, Interdependency of mechanical failure rate of encapsulated solar cells and module design parameters, Proceedings SPIE 8472, Reliability of Photovoltaic Cells, Modules, Components, and Systems IV, Vol. 8472, 84720P SPIE 2012, doi: 10.1117/12.929289.
8. Marco Paggi, Irene Berardone, Andrea Infuso, Mauro Corrado, Fatigue degradation and electric recovery in Silicon solar cells embedded in photovoltaic modules, Scientific Reports 4, Article number: 4506 (2014), doi:10.1038/srep04506.
9. Z.-D. Li *et al.*: Effects of the Curing Process on the Residual Stress in Solar Cell Module, Kem. Ind. 65 (3-4) (2016) 137−146
10. V. Handara, I. Radchenko, S. K. Tippabhotla, K. Narayanan, G. Illya, M. Kunz, N. Tamura, A.S. Budiman, Probing Stress and Fracture Mechanism in Encapsulated Thin Silicon Solar Cells by Synchrotron X-ray Microdiffraction, Solar Energy Mater. & Solar Cells. 162, p. 30-40, 2017.
11. Tippabhotla, S. K., Radchenko, I., Song, W. J. R., Illya, G., Handara, V., Kunz, M., Tamura, N., Tay, A. A. O., and Budiman, A. S. (2017) From cells to laminate: probing and modelling residual stress evolution in thin silicon photovoltaic modules using synchrotron X-ray micro-diffraction experiments and finite element simulations. Prog. Photovolt: Res. Appl., doi: 10.1002/pip.2891.
12. Cullity, B. D. (1978). Elements of X-ray diffraction. 2nd edition. Addison-Wesley: New York.
13. Brent Fultz · James Howe, Transmission Electron Microscopy and Diffractometry of Materials, 3rd Ed., Springer, 2007
14. Kunz, M., Tamura, N., Chen, K., MacDowell, A. A., Celestre, R. S., Church, M. M., ... & Morrison, G. Y. (2009). A dedicated superbend X-ray microdiffraction beamline for materials, geo-, and environmental sciences at the advanced light source. Review of Scientific Instruments, 80(3), 035108.
15. N. Tamura, M. Kunz, K. Chen, R. S. Celestre, A. A. MacDowell, and T. Warwick. A superbend X-ray microdiffraction beamline at the advanced light source. Materials Science and Engineering A-structural Materials Properties Microstructure and Processing, 524:28–32, 2009.
16. A.S. Budiman, Probing Crystal Plasticity at the Nanoscales, Springer, 2015.

17. N. Tamura, H. A. Padmore, and J. R. Patel. High spatial resolution stress measurements using synchrotron based scanning X-ray microdiffraction with white or monochromatic beam. Materials Science and Engineering A - Structural Materials Properties Microstructure and Processing, 399:92–98, 2005.
18. C.Y. Khoo, H. Liu, W. Sasangka, R. I Made, N. Tamura, M. Kunz, A.S. Budiman, C.V. Thompson, C.L. Gan. Impact of Deposition Temperature on the Crystallizations Kinetics of Amorphous GeTe Films. J. Mater. Sci. Soc. 51, p. 1864-72, 2016.
19. A. S. Budiman, K.R. Narayanan, L.A. Berla, N. Li, P. Dickerson, J. Wang, N. Tamura, M. Kunz, W.D. Nix, A. Misra. Plasticity Evolution in Nanoscale Cu/Nb Single Crystal Multilayers as Revealed by Synchrotron X-Ray Microdiffraction. Mater. Sci. Eng. A, 635, p.6-12, 2015.
20. A. S. Budiman, G. Lee, M. J. Burek, D. Jang, S. M. Han, N. Tamura, M. Kunz, J. R. Greer, T. Y. Tsui. Plasticity of Indium Nanostructures as Revealed by Synchrotron X-Ray Microdiffraction. Mater. Sci. Eng. A 538, p. 89-97, 2012.
21. A. S. Budiman, S. M. Han, Q. Wei, P. Dickerson, N. Tamura, M. Kunz, A. Misra. Plasticity in the Nanoscale Cu/Nb Single Crystal Multilayers as Revealed by Synchrotron Laue X-Ray Microdiffraction. J. Mater. Res. 27, p. 599-611, 2012.
22. A.S. Budiman, H-A.-S. Shin, B.-J. Kim, S.-H. Hwang, H.-Y. Son, M.-S. Suh, Q.-H. Chung, K.-Y. Byun, N. Tamura, M. Kunz, Y.-C. Joo. Measurements of Stresses in Cu and Si around Through-Silicon Via by Synchrotron X-Ray Microdiffraction for 3-Dimensional Integrated Circuits. Microelectron. Rel. 52, p. 530-533, 2012.
23. Tamura N. XMAS: A Versatile Tool for Analyzing Synchrotron X-ray Microdiffraction Data, Chapter-4 of Strain and Dislocation Gradients from Diffraction, Imperial College Press London, World Scientific Publishing: Singapore, 2014.
24. E.Gullikson, Center for X-ray Optics, X-Ray Interactions With Matter. (http://henke.lbl.gov/optical_constants/atten2.html) (Last accessed, March 2017).
25. A.S. Budiman et al., “Enabling thin silicon technologies for next generation c- Si solar PV renewable energy systems using synchrotron X-ray microdiffraction as stress and crack mechanism probe” Solar Energy Materials & Solar Cells, 2014, Vol. 130, pp. 303-308.
26. Sasi Kumar Tippabhotla, Ihor Radchenko, Karthic Narayanan Rengarajan, Gregoria Illya, Vincent Handara, Martin Kunz, Nobumichi Tamura, Arief Suriadi Budiman, “Synchrotron X-ray Micro-diffraction – Probing Stress State in Encapsulated Thin Silicon Solar Cells”, Procedia Engineering, Volume 139, 2016, Pages 123-133.
27. ABAQUS Documentation, Version 6.14, SIMULIA, Dassault Systèmes Simulia Corp., 2015.
28. S. K. Tippabhotla, I. Radchenko, W. Song, N. Tamura, A. A. O. Tay and A. S. Budiman, "Effect of interconnect plasticity on soldering induced residual stress in thin crystalline silicon solar cells," 2016 IEEE 18th Electronics Packaging Technology Conference (EPTC), Singapore, 2016, pp. 734-737., doi: 10.1109/EPTC.2016.7861579.

Appendix A: Grain Orientation Maps of the Scanned mc-Si Cell PV Modules

Silicon is an anisotropic crystalline material and hence its elastic properties depend on the grain orientation. The mc-Si solar cells, used in this study have several grains in the µSXRD scanned region (shown in Figure 1(c)). The orientation of the silicon grains with respect to the reference, Silicon (001) plane (aligned with Z direction) for all the scanned samples are shown the Figure A.1. It can be noticed that the crystal plane normals of the grains have different orientations starting from 0^{o} to 45^{o} with respect to the normal to the Si (001) plane. Comparison of the grain orientation maps with the stress maps in Figures 7 and 8 clearly show that the stress contours are influenced by the grain orientations.

However, the high stress in the cell in all the samples is aligned along the lower edge of the interconnect ribbon. Further it can also be noticed that the crystals with different orientations adjacent to the edge of the interconnect get stresses to the same level of stress, irrespective of the grain orientation. This was prominently observed in the stress maps of samples #1-1, #1-2, #1-4 and #2-2. In the samples #1-3 and #2-1, there is mostly one crystal along the lower edge of the ribbon. Which is a clear indication that the high stress is governed by the local banding of the cell near the edge of the interconnect ribbon, which is also in line with the predictions of our finite element simulations, shown in the Figure 10 (f).

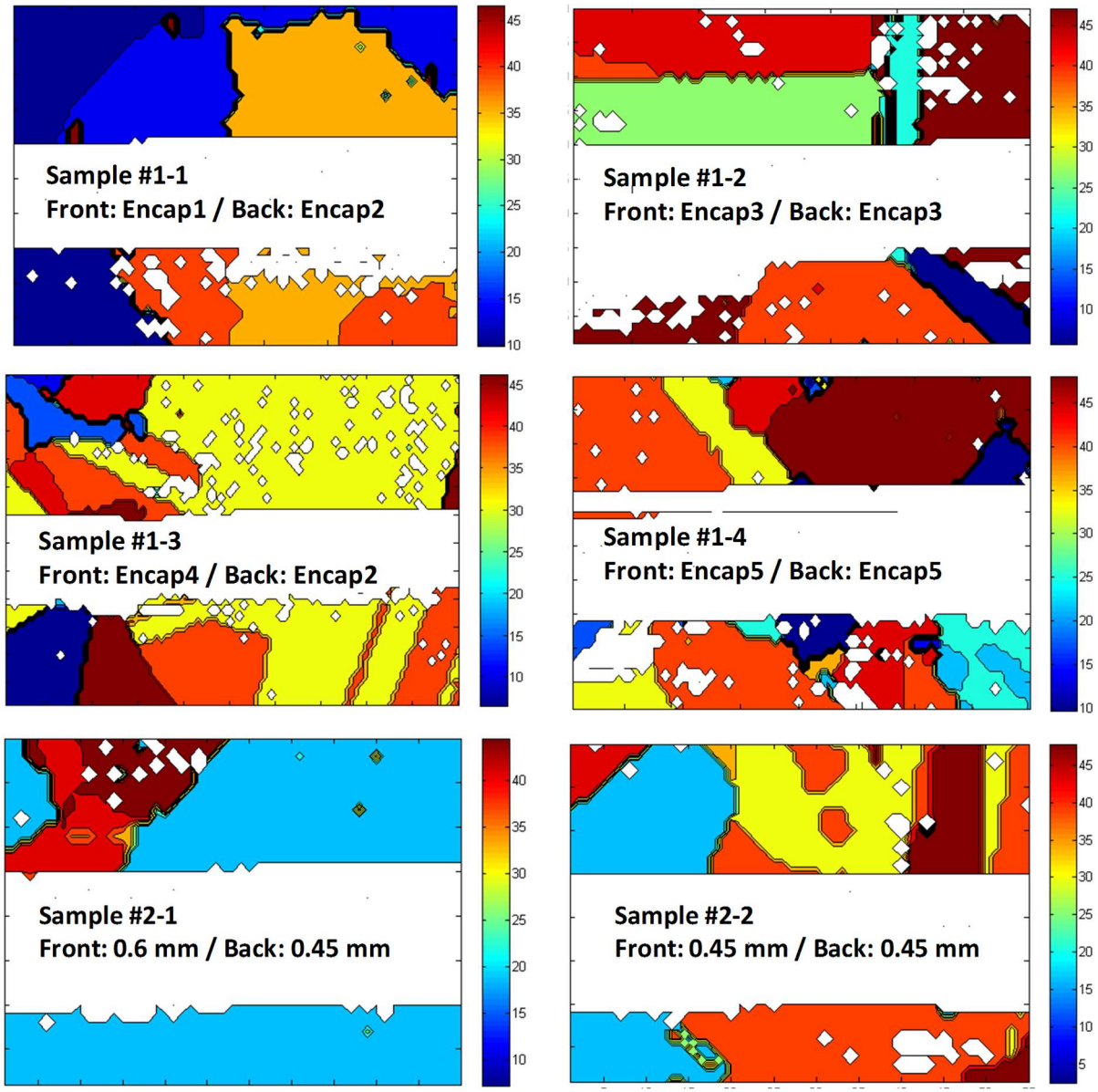

Figure A.1: Grain orientation maps of the µSXRD scanned regions in different mini PV module samples (Note: the white region in the middle of the stress maps indicate no signal from diffraction due to Cu ribbon/ solder). The orientation is expressed as the angle between the normal to the Si (001) plane and the normal to the grain crystal plane.